Excellent specific strength-ductility synergy in novel complex concentrated alloy after suction casting

Materials & Design 242 (2024) 112988

Contents lists available at ScienceDirect

Materials & Design

journal homepage: www.elsevier.com/locate/matdes

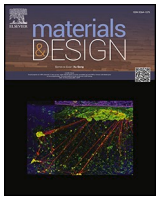

Excellent specific strength-ductility synergy in novel complex concentrated alloy after suction casting

A.R. Balpande [a], S. Agrawal [b], X. Li [c], S. Suwas [b], S. Guo [c], P. Ghosal [d], S.S. Nene [a,*]

[a] Advanced Materials Design and Processing Group, Department of Metallurgical and Materials Engineering, Indian Institute of Technology Jodhpur, Karwar, Jodhpur, Rajasthan 342037, India
[b] Laboratory for Texture and Related Studies, Department of Materials Engineering, Indian Institute of Science, Bangalore, Karnataka 560012, India
[c] Department of Industrial and Materials Science, Chalmers University of Technology SE-41296 Gothenburg, Sweden
[d] Electron Microscopy Group & Advanced Materials Characterization Center, Defense Metallurgical Research Laboratory, DRDO, Hyderabad 500058, India

ARTICLE INFO

Keywords:
Complex concentrated alloy
Suction casting
Specific strength
Valence electron concentration
Strength-ductility synergy
Void formation
Deformation bands

ABSTRACT

Lightweight alloys are known to improve the fuel efficiency of the structural components due to high strength-to-weight ratio, however, they lack formability at room temperature. This major limitation of poor formability is most of the time overcome by post-fabrication processing and treatments thereby increasing their cost exponentially. We present a novel $Ti_{50}V_{16}Zr_{16}Nb_{10}Al_5Mo_3$ (all in at. %) complex concentrated alloy (Ti-CCA) designed based on the combination of valence electron concentration theory and the high entropy approach. The optimal selection of constituent elements has led to a density of 5.63 gm/cc for Ti-CCA after suction casting (SC). SC Ti-CCA displayed exceptional room temperature strength (UTS ~ 1.25 GPa) and ductility (ε ~ 35 %) with a yield strength (YS) of ~ 1.1 GPa (Specific YS = 191 MPa/gm/cc) without any post-processing treatments. The exceptional YS in Ti-CCA is attributed to hetero grain size microstructure, whereas enormous strength-ductility synergy is due to the concurrent occurrence of slip and deformation band formation in the early stages of deformation followed by prolonged necking event due to delayed void nucleation and growth. The proposed philosophy of Ti-CCA design overcomes the conventional notion of strength-ductility trade-off in such alloy systems by retaining their inherent characteristics.

1. Introduction and design framework

Lightweight alloys have a good specific strength; however, they exhibit a common limitation of very poor tensile ductility at room temperature (RT) in as-cast conditions. Typical conventional lightweight alloys such as Ti-6Al-4V or Ti-5553 alloys displayed very high specific strength, but their reasonable ductility is only achieved after the post-fabrication of as-cast alloys by implementing thermomechanical treatments [1,2]. The mechanical properties of these light metal alloys is proven to improve by adding reinforcements like carbon nanotubes (CNTs). However, this increases the fabrication cost and time and can lead to unidirectional properties [3–5]. A similar trend is seen for conventional refractory elements-based alloys, most of which need some post-fabrication treatments to attain some fair plasticity level in them [6,7]. In addition, casting is seen as a primary issue due to their high melting points, as they are typically fabricated using the powder metallurgy route.

The inclusion of alternative fabrication routes not only increases the cost of the already expensive alloys but also makes them very fragile for operations such as machining and cutting. Many attempts were made to overcome these issues including the development of metastable Ti alloys which essentially merge the lightweight alloy design with refractory alloy design since major alloying addition in this design strategy includes the addition of refractory elements such as V, Nb, and Mo in a lightweight matrix of Ti. Ti-7.5Mo alloy is a classic example in this direction which displayed a very high strength (1.1GPa) at a total elongation of 30 % in the as-cast state. The only issue, in this case, is a low YS of ~ 550 MPa which has limited its applications due to poor safety considerations [8]. The introduction of the complex concentrated alloy concept to the metallurgical community has provided a new pathway for looking at the alloy design. Fewer attempts were made to merge CCA design theory with conventional metastable Ti alloy design [9].

The introduction of multiple alloying additions (CCA design principle) in the Ti matrix was tried based on molybdenum equivalence (MoE)

* Corresponding author.
E-mail address: ssnene@iitj.ac.in (S.S. Nene).

https://doi.org/10.1016/j.matdes.2024.112988
Received 22 February 2024; Received in revised form 18 April 2024; Accepted 28 April 2024
Available online 29 April 2024

[10] and valence electron concentration (VEC) theory [11] individually wherein β phase stability is engineered for obtaining good strength-ductility synergy while not compromising the YS of the material. In similar lines, Huang et. al. [6] reported YS of 800 MPa with UTS and ductility of ~ 1.1 GPa and 22 % respectively for as-cast $TiZrHfTa_{0.6}$ complex concentrated alloy which they mainly attributed to the transformation-induced plasticity (TRIP) in the alloy at RT [6]. However, this simultaneous increase in YS, UTS, and ductility was at the expense of an immense increase in the average cost and density of the alloy due to the huge presence of expensive and heavy elements like Hf and Ta. A recent attempt was made by Zhang et al. [12] to obtain a cost-effective solution to this problem wherein Ti-rich alloy containing very cost-friendly elements such as Al, Cr, Fe, and V are added displaying YS of 1057 GPa and UTS of ~ 1.2 GPa but at the expense of a decrease in ductility to 6.5 % in as-cast state.

Fig. 1(a) shows the decision path of alloy design which involves multi-filtering methodology used for alloy system formulation in this work.

1. The first step in the procedure was filtering out elements based on the MoE theory used for designing metastable and stable β-Ti complex alloys [10]. The elements that have very high multiplicity factors in the MoE equation (Fig. 1(a_1)) are strong β eutectoid stabilizers and hence they are sieved out in this step which thus makes Mo, V, W, Nb, Ta, Hf, Sn, Zr, Si and Al as available elements to select for the new alloy system.
2. In the second step, solubility of these remaining elements is studied in the β-Ti phase field [13] (i.e. above the β-transus in corresponding binary phase diagrams with Ti) and based on that, Si and Sn are taken out from the list of available elements.
3. The third step applies the density filter to remain aligned to obtain an alloy with a density of less than 6 g/cc [13]. As a result, very heavy elements like W, Ta, and Hf are filtered out from the list of Mo, V, W, Nb, Ta, Hf, Zr, and Al (Fig. 1(a_3)). As a result of this step, a system to be designed is fixed to Ti-Zr-V-Nb-Al-Mo.
4. The fourth step used is very critical since it involves fixing the amounts of the major constituent elements such as Nb, V, Zr, and Al in a matrix of 50 % Ti alloy based on the valence electron concentration (VEC) theory. We started fixing the amount of the proposed elements by taking the reference system as $Ti_{50}Zr_{12.5}V_{12.5}Nb_{12.5}Al_{12.5}$. We performed a detailed analysis of VEC for as-cast Ti alloys including conventional as well as complex alloys (having Ti content > 45 at. %) as shown in Fig. 1(a_4) and found that SDI vs VEC follows a Gaussian type of distribution ($r^2 = 0.99$). The detailed equation of the curve is present in the Supplementary Document Table S2. having a peak of SDI in the VEC range of 4.22 to 4.35 for the as-cast Ti rich alloys [12,14–27]. The complete study is available in the Supplementary Document Table S1. The VEC calculations are made as per the Eq. (1), [11]

$$VEC = \sum_{i=1}^{n} c_i . (VEC)_i \quad (1)$$

Where, *VEC*: valence electron concentration, c_i: atomic fraction of element *i* in the matrix, and *(VEC)i*: valence electron concentration of the i^{th} element. Thus, we fixed a region of interest as marked in Fig. 1(a_4), and in line with that, we started optimizing the VEC value by compositional variation in the $Ti_{50}Zr_{12.5}V_{12.5}Nb_{12.5}Al_{12.5}$ alloy system.

As the VEC of the reference alloy was found to be very low (4.125), we increased the content of V and Zr both by 2.5 at. %, at the expense of Al and Nb, making the new alloy composition as $Ti_{50}Zr_{15}V_{15}Nb_{10}Al_{10}$ and having a VEC of 4.15. We chose to decrease Nb and Al at the expense of Zr and V with the same amounts to have negligible variation in density while having substantial change in VEC as shown in supplementary Fig. S1. As VEC showed a increasing trend with this compositional variation, we further tried to modify the composition by reducing the Al content by 2 at. % at the expense of both Zr and V since Al is the most influential element in the alteration of VEC [11] than the rest of the other elements in the reference system. Moreover, Al is the only element in the proposed alloy system that has

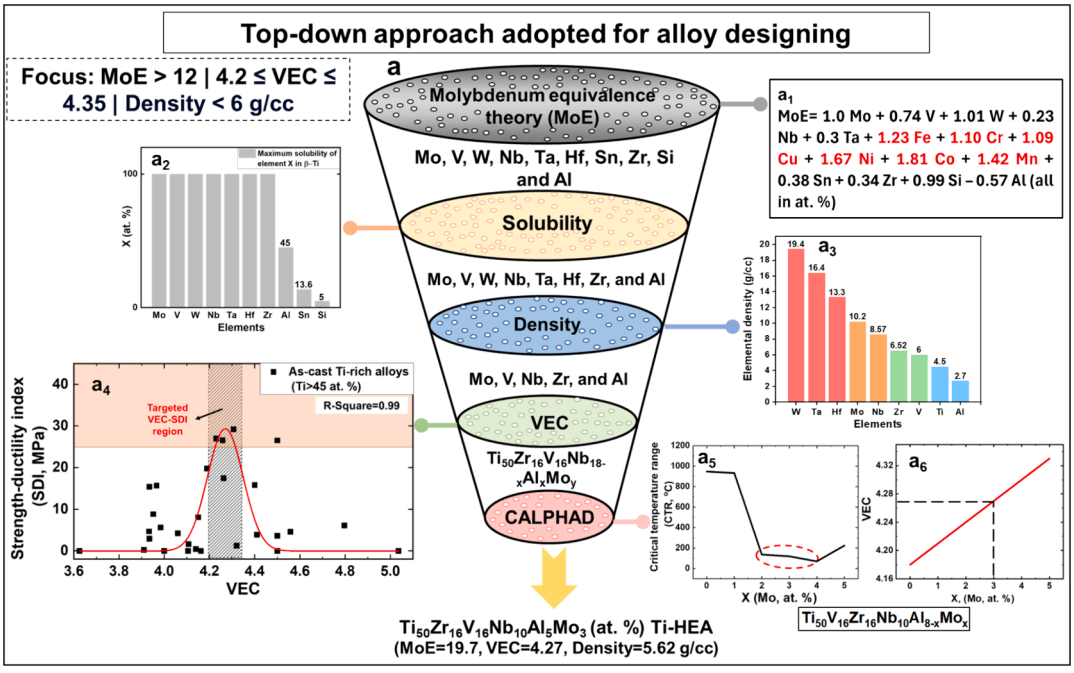

Fig. 1. (a) Decision path for alloy design of Ti-CCA, (a_1) Molybdenum equivalence (MoE) equation, (a_2) Maximum solubility of an element in the β-phase field of binary alloy with Ti, (a_3) Density of all elements soluble in β-Ti, (a_4) Strength-ductility index (SDI) vs valence electron concentration (VEC) of the pre-existing Ti-rich alloys (Ti > 45 at. %) in as-cast condition [12,14–27], (a_5) critical temperature range (CTR) as function of increase in Mo content at the expense of Al in $Ti_{50}Zr_{16}V_{16}Al_{8-x}Mo_x$ (at. %) alloy.

solubility < 50 % in β-Ti and thus decreasing its amount reduces the chances of IMC formation upon melting [11]. However, we reduced Al content to a minor amount to satisfy the density requirements in the targeted range. This compositional change led to the next variant of the alloy $Ti_{50}Zr_{16}V_{16}Nb_{10}Al_8$ but having a very sluggish increase in VEC to 4.18 and a further decrease in Al can increase the VEC but at the expense of a significant increase in density (Fig. S1).

These compositional variations suggested that the targeted VEC range can only be achieved by the addition of such an element whose minor addition can lead to a major change in VEC without a rapid increase in density (Fig. S1). Moreover, it should be almost 100 % soluble in β-Ti. As a result, we decided to introduce Mo into the $Ti_{50}Zr_{16}V_{16}Nb_{10}Al_8$ alloy to reach the VEC value > 4.22. Mo is also a very strong grain refiner and alters the critical temperature range (CTR) [28] of most of the Ti-based alloys drastically which is desired to have defect-free castings. Hence, the Mo content in the alloy is fixed by considering CTR, VEC, and density simultaneously. As we wanted to have a minor addition of Mo, we decided to have it at the expense of Al due to the high sensitivity of later to the alteration of VEC and its lower solubility in β-Ti.

5. The $Ti_{50}Zr_{16}V_{16}Nb_{10}Al_{8-x}Mo_x$ alloy system is further studied using the CALPHAD approach (Thermo-Calc-based TCHEA6 database) to identify the optimal amount of Mo content (x) to be added in the alloy system. This is tried by studying the effect of Mo addition on the Scheil solidification curve, i.e., on CTR [28]. As CTR decides the ability of the alloy to suppress the solidification cracking because of solute enrichment in the last liquid getting solidified, minimum CTR is preferred for defect-free solidification. Moreover, smaller CTR also indicates lesser solute partitioning among solid and liquid phases towards the end of solidification which in turn leads to a planar solidification front. As a result, alloys with low CTR solidify very similarly to pure metals, i.e., by planar solidification mechanism. Planar solidification in polycrystalline materials (pure metals) promotes equiaxed morphology at the end of casting which is preferential for obtaining isotropic mechanical properties. Hence, it is expected that alloys with low CTR can show equiaxed microstructure after complete solidification [29].

In line with this, Scheil's simulations with Mo content showed a very interesting behavior. The CTR of the $Ti_{50}Zr_{16}V_{16}Nb_{10}Al_{8-x}Mo_x$ alloy system is found to initially decrease dramatically from almost 1000 °C to ~ 100 °C when Mo is varied from 0 to 4 at. % (Fig. 1(a_5)). However, there is a sudden increase in CTR again with the increase in Mo content beyond 4 at. % taking it closer to 200 °C (Fig. 1(a_5)). Thus, to obtain equiaxed solidification in the designed alloy composition, we preferred to have Mo content from 3 to 4 at. % based on the analysis shown in Fig. 1(a_5). However, Mo is also a very crucial element in altering the VEC and density of the alloy (as per Fig. 1(a_3 and a_4)) and hence final tuning of Mo content is again performed by doing the VEC and density calculations. Based on these evaluations, 3 at. % Mo is found to be optimal to keep the VEC and density of the proposed alloy in the targeted range as shown in Fig. 2. Hence, the alloy composition is fixed to $Ti_{50}Zr_{16}V_{16}Nb_{10}Al_5Mo_3$ (hence-forth designated as Ti-CCA), and it was chosen for the study.

2. Experimental

2.1. Material and processing

$Ti_{50}Zr_{16}V_{16}Nb_{10}Al_5Mo_3$ (henceforth designated as Ti-CCA) is produced from high-purity metals (>99.9 %), with each alloying element sectioned into smaller pieces beforehand, and the weight was confirmed to have an accuracy of 0.005 g. Specimens were prepared with arc melter (Edmund Bühler GmbH, Germany), operated in a Ti-gettered high-purity argon atmosphere with a prior vacuum of order of 10^{-5} mbar. The melting of each metallic button was repeated at least five times, with specimens being flipped after each melting, to achieve good macroscopic chemical homogeneity. Obtained alloy buttons were drop cast into a 10 × 10 × 45 mm^3 copper mold. The casting mold and melting plate on which the raw material was placed, are made from copper to conduct the heat quickly. The casting chamber and the crucible plate are also water-cooled by an external chiller to avoid overheating during the melting process. The average density (measured using Archimedes principle) of the alloy was measured to be 5.63 gm/cc after casting.

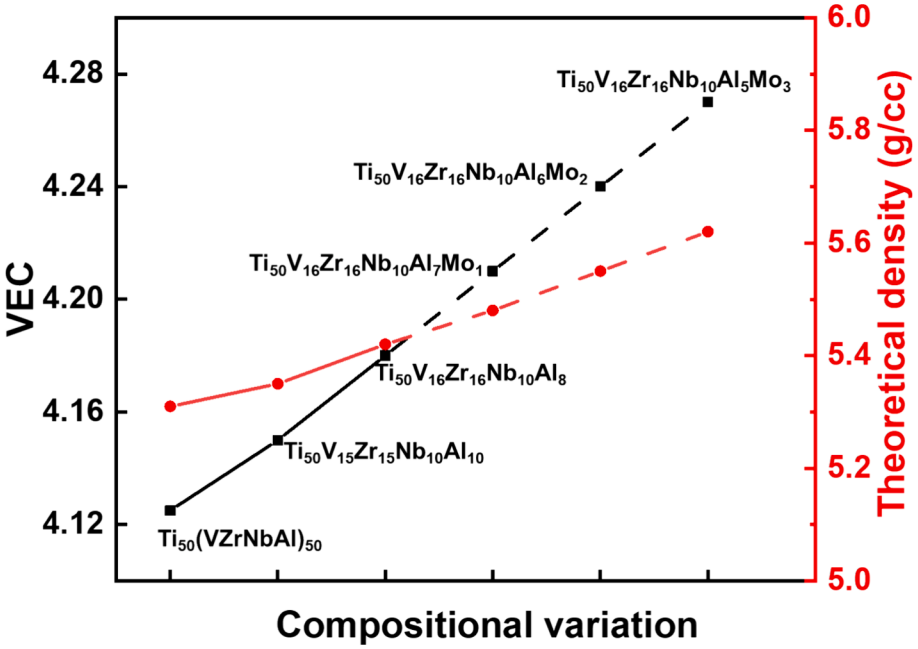

Fig. 2. VEC and theoretical density change as a function of compositional variation in $Ti_{50}Zr_{16}V_{16}Nb_{10}Al_{8-x}Mo_x$ alloy system.

2.2. Microstructural and mechanical characterization

The X-ray diffraction (XRD) measurement was performed using RIGAKU X-ray equipped with Cu K_α source at 40 kV and 30 mA with a step size of 0.1 degrees at a scan rate of 1 degree per minute. The microstructure was analyzed by various methods and at various locations. For microscopy, the samples were electropolished using the electrolyte solution (90 ml dist·H_2O, 730 ml ethanol, 100 ml butoxy ethanol solution mixed with 78 ml perchloric acid) using Struers electropolishing setup for 20 s at constant (2.1 A, 40 V) power supply. The Backscattered electron (BSE) imaging and energy-dispersive spectroscopy (EDS) were done using Zeiss Gemini 450 scanning electron microscope (SEM). The microscope was equipped with the EDAX octane elite and velocity detectors to obtain nearly accurate EBSD results. The step size used varied from 50 nm to 2 μm based on the requirements for the analysis. The EBSD data was analyzed using the TSL OIM V8 software. Fracture surface imagaging is carried out after complete tensile testing using same FE-SEM system to know the fracture modes in detail. All the specimens were ultrasonically cleaned before they are imaged for fractography. The transmission electron microscopy (TEM) was carried out in FEI Tecnai 20 with EDS at 200 kV. Samples are prepared with FIB (to take out samples from specific area) and a precision ion polishing system (PIPS) to thin down to electron transparency using ions to TEM thickness (a few nanometers thickness with a hole in the center), where TEM is carried out at 200 kV.

For the tensile study, dog bone-shaped samples with a gauge length of 2 mm, width of 1 mm, and thickness of 1 mm were machined from the center of the ingot using wire electrical discharge machining. The detailed dimensions of the sample can be seen in the attached Supplementary Document (refer to Fig. S2). The samples were tested on a Tinius-Olsen ST25 universal testing machine (UTM) equipped with a 25 kN load cell. In each condition, three samples were tested at room temperature and an initial strain rate of 10^{-3} s^{-1} to confirm the reproducibility of the results (refer to Fig. S3 for Supplementary Document).

X-ray microscopy (XRM) is performed on fractured tensile specimens of SC Ti-CCA using a Zeiss Xradia Versa 520 microscope. A full field-of-view scan at a magnification of 4X and an interior tomography at a higher magnification of 20X were carried out to image the fractured tensile specimen and detailed fracture surface, respectively. Voltage and power, exposure time, and source-to-detector distances were optimized and selected based on the requirement. In each case, the filter was selected by checking the transmittance at the angular position of 45°. The initial transmittance was recorded for the air filter. Based on this transmittance value, an appropriate filter was selected to increase transmittance in the range of 20–35 %. The analysis of the obtained XRM data was done using the Dragonfly software.

3. Results and discussion

3.1. Microstructure and phase analysis

Fig. 3(a) shows the Scheil solidification curve obtained from the Thermo-Calc TCHEA6 database for the designed composition which clearly shows that the critical temperature range is very small (~120 °C) which is almost 100 °C less than conventional Ti-6Al-4V alloy indicating a higher tendency to undergo planar solidification in former. Electron back scattered diffraction (EBSD) inverse pole figure map (Fig. 3b) clearly shows the formation of equiaxed grain morphology of the SC Ti-CCA. Moreover, the microstructure displayed a heterogenous distribution of grains with the finest grain of d_{avg} ~ 5.9 μm in the matrix of very coarse grains d_{avg} ~ 353 μm with no preferred texture irrespective of their sizes as confirmed by Fig. 3(b). The overall grain distribution is seen in the Supplementary Document Table S3. To understand the phase formation in the state, EBSD and the X-ray diffraction (XRD) analysis are performed as shown in Fig. 3(c, d) which show formation of heterogenous grained β-b.c.c. microstructure which is further supported by the major peaks of the β-Ti (b.c.c.) phase in XRD. A minor peak of Zr containing β (b.c.c.) phase (card details present in the Supplementary Document) is also captured in XRD and to confirm the formation of two compositionally different phases we performed the energy dispersive spectroscopy-based X-ray mapping as shown in Fig. 3(e).

Fig. 3(e) shows the secondary electron image of the SC specimen

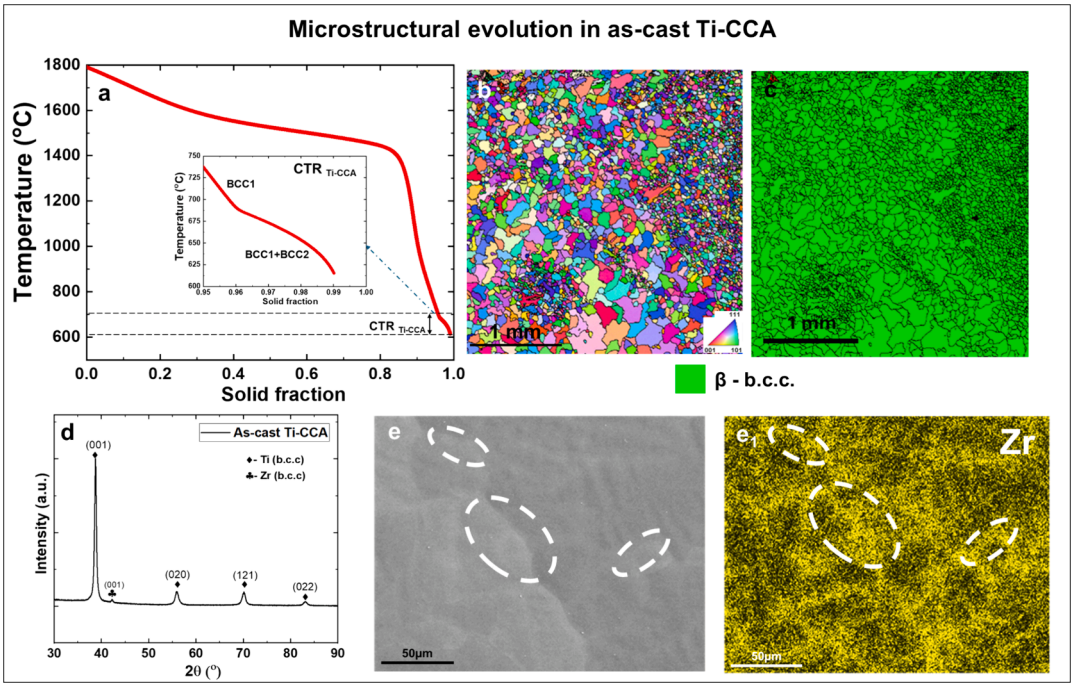

Fig. 3. (a) Scheil's solidification behavior showing the critical temperature range for Ti-CCA, (b) IPF map showing the absence of any preferential orientation in SC microstructure, (c) Phase map showing SC microstructure, (d) XRD pattern showing the presence of β-Ti and Zr containing b.c.c. phase in the SC microstructure of Ti-CCA, (e) EDS X-ray mapping showing the Zr separation at the grain boundaries.

along with the corresponding X-ray maps for Zr (Fig. 3(e_1)). Grain-to-grain mapping (as shown in Fig. 3(e, e_1)) reveals severe grain boundary presence of Zr. The complete X-ray mapping can be seen in the Supplementary Document Fig. S4. As per literature [13], all constituent elements such as V, and Nb (except Al) are strong β stabilizers in both Ti as well as Zr and hence resulted in overall stability of the β −b.c.c. dominated microstructure in Ti-CCA in spite of pronounced Zr splitting at the grain boundaries (Fig. 3(e)). The lattice parameters of Zr-rich and Ti-rich b.c.c. phases were 3.025 and 3.286 Å respectively with Zr-rich b.c.c. phase nearly equal to 3 vol% thus making it tough to distinguish them in the EBSD phase map.

It is also important to note that, the microstructure of Ti-CCA in the SC condition is not conventional dendritic but throughout the cross section it showed equiaxed morphology with severe grain size distribution irrespective of varying thermal gradients and solidification rate. The grain size distribution (fine colonies in the matrix of coarse grains) appears to be the result of the combined effects of temperature gradients and the sluggish diffusivity of Zr in Ti-Zr-V-Nb-Mo containing alloys [30]. As predicted by the solidification curve in Fig. 3(a), a smaller CTR gives more opportunity to solidify the alloy with a planar interface in conventional cooling rates. We examined this by melting the alloy with three methodologies.

In the first, the alloy is melted in a conventional Cu crucible (non-confined crucible melting), and in the second one, it is melted in a cavity created in a Cu crucible (confined crucible melting). In these two cases, the major difference is the change in gradients since in cavity-based solidification, the cooling occurs from all three sides whereas in a conventional crucible, it mainly happens only at the bottom where the ingot touches the Cu wall. In the suction casting method, cooling not only happens from all 6 sides but also occurs at a high rate. As a result, we get equiaxed morphology in all three cases but the most heterogeneous grain size distribution is obtained in suction casted alloy compared to other cases. The details of these are shown in Fig. 4. As a result, the equiaxed microstructure formed in Ti-CCA is an inherent nature of the alloy system, and changes in casting methodology may only result in a change in the grain size distribution in the microstructure with minor changes in fractions of Zr containing b.c.c. phase.

3.2. Stress–strain response

Fig. 5 shows the overall tensile behavior of Ti-CCA at RT in the SC condition. It is very clear from Fig. 5(a) that Ti-CCA has shown exceptional strength-ductility synergy demonstrated by true stress-true strain curve when compared to other conventional Ti alloys such as Ti-6Al-4 V, and recently developed Ti alloys [1,12]. Interestingly, two distinct regions of strain hardening and softening were seen with the onset of necking in Ti-CCA.

The work hardening (WH) curve of Ti-CCA (Fig. 5(b)) resembles most of the f.c.c.-based transition metal CCAs where the WH rate (WHR, θ) has sustained above 1000 MPa (refer. Supplementary Doc Fig. S5 [31–33]. The sustainment of WHR at a strain level of more than 5 % indicates deviation from conventional slip-dominated deformation to non-conventional modes such as twinning or transformation-based deformation [1]. The formation of a hump in the WHR rate curve within a strain regime of 10–15 % moreover points towards an extensive local increase in the stress required for the deformation. Thus, it is expected that Ti-CCA has multiple deformation modes active at RT in the SC state itself providing it with the ability to harden while retaining the plasticity. Fig. 5(c) shows the pre and post-deformation pole figures for $\{0\,0\,1\}_\beta$, $\{0\,1\,1\}_\beta$, and $\{1\,1\,1\}_\beta$ textures. There appears substantial change in texture intensity from 1.36 to 5.42 after deformation which is mainly attributed to lattice rotations during deformation as marked in Fig. 5(c).

It is reported that plastic deformation i.e., changes in the shape of the metal/alloy can be related to the valence electron concentration (VEC) and is purely a compositional property [34]. Higher VEC implies stronger metallic bonding and hence more difficulty in deformation. As a result, HCP alloys that have the highest VEC in the range of 8.25–8.5 show immense difficulty [30] in deformation, whereas BCC alloys show easy deformability owing to lower VEC. Within this broader range of VEC, we found that Ti alloys (having Ti content > 45 %) having VEC values within a narrower range of 4.2–4.35 display high SDI values (Fig. 1(a_4)) thereby following a classical gaussian distrubution.

Based on this, Ti-CCA designed in the present investigation, exhibits a VEC of 4.27 which thus falls in the range of strong and ductile β-Ti alloys regime [12,14–27,34], thus rendering it ductile. Ti-CCA showed a

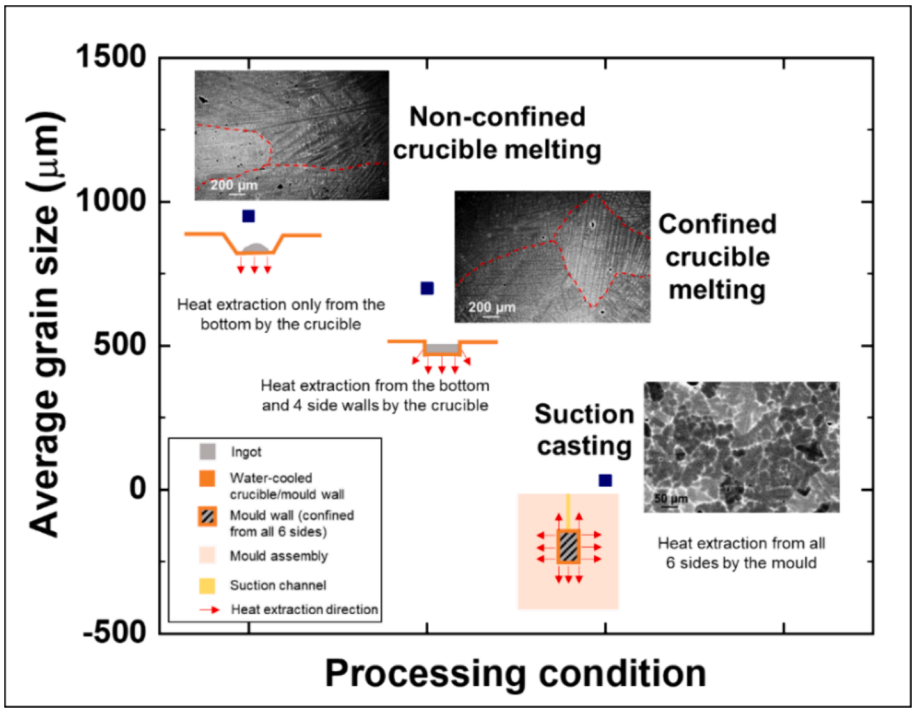

Fig. 4. Grain size and morphology variation as a function of the fabrication method (processing condition).

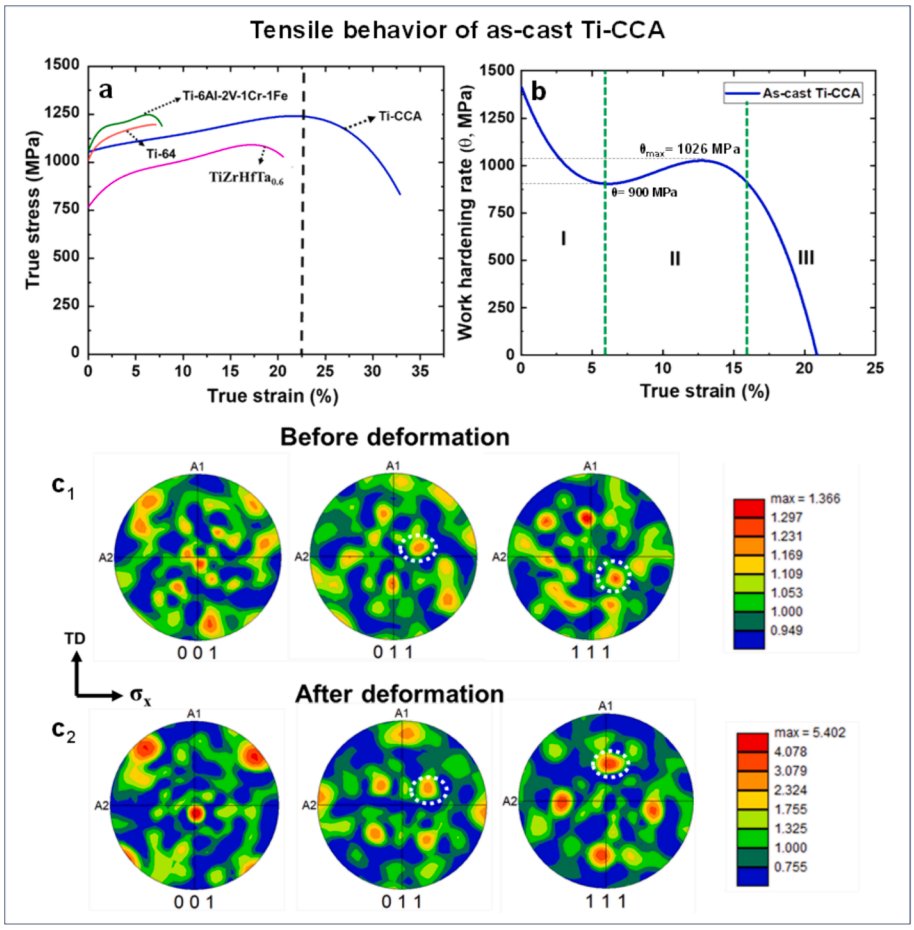

Fig. 5. (a) True stress-true strain curve for Ti-CCA in SC state deformed at RT and strain rate of 10^{-3} s^{-1} [1,12], (b) work hardening curve for Ti-CCA in the SC state showing different stages of WH, (c_1, c_2) Texture analysis for pre and post deformation microstructures of Ti-CCA.

MoE value of 19.73 which as per the discussion by Wang et al. [7] indicates extreme β stability and matches with the observed microstructural evolution in the SC state. Thus, a combined consideration of VEC and MoE has led to the design of Ti-CCA with adequate deformation response [35]. A detailed discussion of the experiments to investigate the deformation behavior of Ti-CCA is given subsequently.

3.3. *Tensile flow hardening: Deformation mechanisms*

It is important to first note the extremely high yield strength (YS ~ 1 GPa) for Ti-CCA in a suction casted condition. This high YS of SC Ti-CCA is a result of having almost more than 30 % fraction (Fig. 6(a)) of fine grains (highlighted with white colour in Fig. 6a1) having sizes ranging from 5 to 55 μm and very little volume (~5.6 %, Fig. 6(a)) of extremely coarse grain sizes (~200 – 375 μm) in the SC microstructure (highlighted by small white dotted line in Fig. 6(a_1)). Moreover, the presence of Zr segregation at the grain boundary (Fig. 3(d_1)) helps in the refinement of microstructure during SC which supports the presence of a higher finer grain size region thereby providing excellent YS to the alloy by Hall-Petch strengthening. The details of grain size distribution are

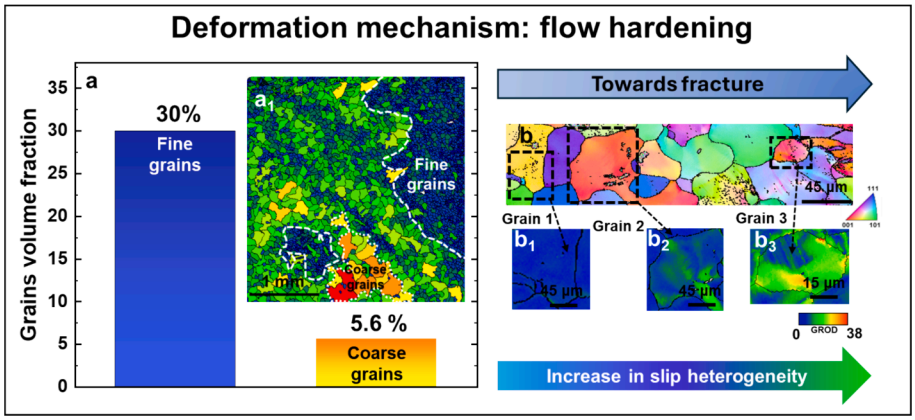

Fig. 6. (a) Average grain distribution in the SC Ti-CCA with the reference micrograph covering the grain distribution, (b) Inverse pole figure (IPF) along with (b_1-b_3) Grain reference orientation deviation (GROD) maps of selected grains as marked in Fig. 6(a).

given in supplementary files for reference. Heterogeneous grain size distribution can also help in maintaining the strength-ductility balance by effective stress partitioning among different-sized grains. The fine grains help in providing strength whereas small grains assist in accommodating deformation. Thus, the presence of a heterogenous grain structure is also beneficial in contributing to an overall increase in work hardening ability of Ti-CCA in SC condition.

The subsequent thing to note is the significant flow hardening and steady flow softening before the tensile failure in the true stress–strain curve of Ti-CCA. Such a deformation response itself is very uncommon in most of the recently designed strong and ductile Ti-based complex alloys and thus we investigated the post-deformation microstructures as shown in Fig. 6(b). To understand the primary deformation mode during flow hardening, we performed low magnification EBSD mapping of the gauge section which captured the region from a less deformed zone to a fracture tip. It is evident from the IPF map that the deformation is predominantly accommodated by slip and there are no traces of twins or martensite/ ω laths in the deformed region.

The texture analysis before and after deformation suggested substantial grain rotations (Fig. 6(b)) during deformation which is a necessary step taken by the material to maintain a minimum of 5 slip systems for continuing the deformation when other mechanisms such as twinning or transformation are not present [36–38]. However, the distinct sustainment of WH rate over the 10–15 % plastic strain in the WH curve (Fig. 5(b)) indicates activation of additional deformation modes than just slip during deformation. To understand the finer microstructural attributes of deformation, 3 grains were identified as highlighted by the black squares, and the strain distribution within each of these three grains was obtained using the grain reference orientation deviation (GROD) analysis (Fig. 6(b)). The misorientation line analysis within each of these grains suggested a local increase in the misorientation indicated by the increase in GROD value for grain 1 to grain 3 respectively, indicating a substantial increase in slip heterogeneity within the grains as a function of straining. The local increase in the misorientation caused by heterogeneous slip events can lead to dislocation rearrangements and can form deformation bands (DBs) in b.c.c. materials. The main driving force for the formation of such DBs during the deformation is slip heterogeneity within the grains which is captured by the GROD maps in Fig. 6b [36–40].

Fig. 7(a–a_4) show the trace analysis performed on such DBs formed in 3 different grains to understand their slip character. Trace analysis on these grains confirmed that these bands are predominantly parallel to $\{110\}_\beta$ planes of the β-b.c.c. matrix. Fig. 7(b) shows the bright field TEM image corresponding to the $[001]_\beta$ zone axis from the gauge region of the deformed specimen. Fig. 7b1 further confirms the formation of a deformation band having an approximate size of 200 nm in the deformed specimen having a similar slip character as shown by EBSD analysis earlier. It is further important to note that, the absence of change in crystal structure or spot splitting in the corresponding selected area diffraction (SAD) pattern (Fig. 7(b_2)) also validates that no phase or twin transformation occurred during deformation. Fig. 7(a_4) shows the EBSD image quality (IQ) map of the deformed region which clearly shows grain fragmentation. Detailed EBSD analysis of the selected region from the IQ map shows a zone that appears like a twin in the grain but has a local misorientation (θ) at the twin-like feature/ parent grain interface to be 4° (shown in supplementary document, Fig. S6). This further supports the formation of $\{1\,1\,0\}_\beta$ DB with a size of around 7–8 μm. Further, sub-grains having local misorientations of less than 15° have started forming within such DBs as as shown in Fig. 7(a_4).

As suggested by EBSD as well as TEM investigations, the absence of twin/transformation traces indicates sustained WH over $\Delta\varepsilon_{sustained}$ is a result of strain energy minimization by the formation of deformation bands (DBs) [27,41]. Such DBs are seen with TEM and EBSD analysis as marked in Figs. 6 and 7 clearly. These DBs and sub-grains themselves can act as barriers to dislocation motion as the deformation continues and can cause a local increase in stress required for deformation by the dynamic Hall-Petch effect [40]. Moreover, the presence of heterogenous grain size distribution helps in effective load transfer during deformation thereby maintaining the strength-ductility synergy over a wide range of strains [42–44]. The presence of dislocation motion obstacles such as DBs and grains of varying diameters causes a local increase in stress required for deformation which is captured in the WH curve in the form of a hump formed over the strain levels of 10–17.5 %. Thus, the deformation in SC Ti-CCA within the sustained regime is mainly

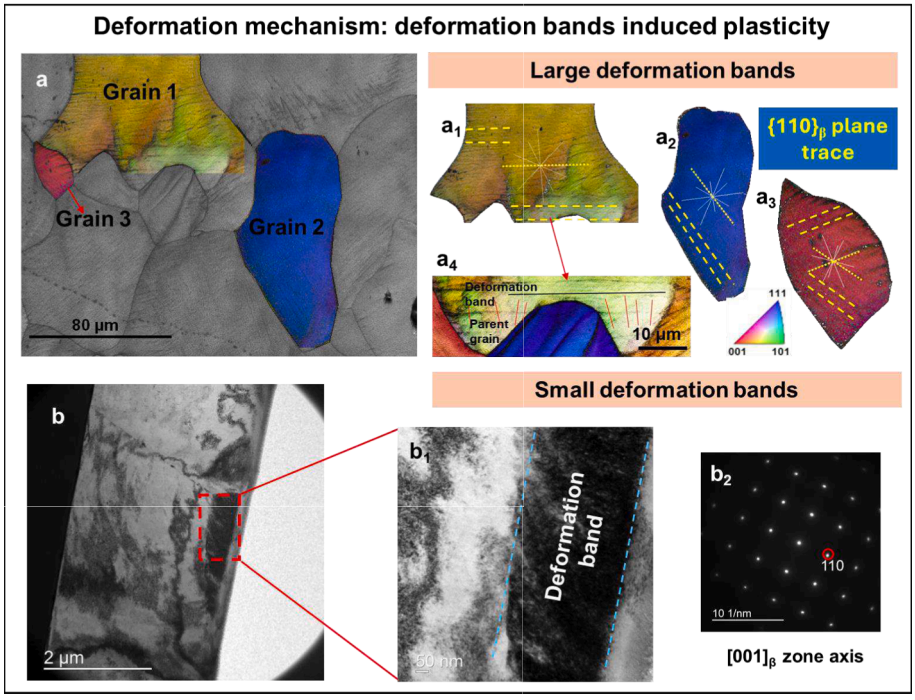

Fig. 7. (a) EBSD IQ map of deformed specimen showing the highlighted grains, (a_1,-a_4) Selected grains for trace analsyis, (b-b_2) Bright field TEM images and corresponding selected area diffraction pattern for deformed specimen.

accommodated by two events namely the heterogeneous grain size distribution and WH activity at the DB/matrix interfaces (formation of a hump in sustained WH regime) respectively. Thus, the concurrent presence of slip and formation of DBs led to significant strain hardening in SC Ti-CCA.

3.4. Tensile flow softening: Fracture mechanisms

Further, the substantial softening observed in the stress–strain curve of Ti-CCA (Fig. 5(a)) must be associated with the pronounced diffused necking behavior beyond the point of instability [45]. Fig. 8(a) shows the 2D reconstruction of the entire gauge region after performing X-ray microscopy (XRM) which shows a very pronounced cone-shaped feature of the fractured tip. The marginal drop (5.5°) in vertical gauge angle on either side of the gauge region (marked by dotted yellow lines in Fig. 8 (a)) suggests very steady progress of the necking event in the specimen during deformation. This sustained flow softening displayed in the stress–strain behavior is evidence of not only delayed plastic instability but also low-stress triaxiality during later stages of deformation. The details of this region are seen in Fig. 8(b).

The overall nature of the fracture appears to be in a mixed mode wherein dimples, as well as river line features, are seen at higher magnification imaging of the fracture surface as shown in Fig. 8(c). A detailed investigation of fracture modes was carried out from fractographic analysis and it was found that the dimples (D), quasi-cleavage (QC) as well and cleavage (C) are the primary modes of failure. Volume fraction calculations (Fig. 8(c)) of these modes from the fractographic micrographs show that most of the fraction is occupied by D mode and almost similar fractions are present for QC and C mode which suggest that softening is not sudden but steady. This is also supported by the presence of a 45° angle in the fractured tip (green dotted lines in Fig. 8(b)) with the tensile loading direction (i.e. with the gauge length) in the central region whereas 20° tilt from the loading direction at the edges of the fracture tip thereby suggesting the gradual defect propagation (ductile) at the central part and sudden fracturing (near brittle) at the edge [46,47]. To understand the steady flow softening behavior further, we performed some detailed analysis using XRM which is discussed subsequently.

According to the fracture theory, void nucleation mainly happens in the region of necking due to stress localization and change of stress state [47,48]. It is also understood that, if the grains have high/low aspect ratios (columnar morphology of grains), it promotes easy void nucleation followed by their coalescence leading to early fracture [47,48]. If the stress triaxiality can be maintained low during tensile deformation, the void nucleation can be minimized. Moreover, if the voids form, they reach the void growth saturation well before the void coalescence begins and thus can delay the fracture. Hence, maintaining low-stress triaxiality throughout the gauge is the key to having sustained softening behavior during deformation. A minor fraction of the second phase/deformation obstacles (bands, twins, etc) also assists in minimizing the stress triaxiality promoting sites and thus can help in the steady necking of the sample [48].

In line with that, with the equiaxed morphology of grains in SC Ti-CCA, the void nucleation by decohesion at the grain boundary can be minimized suggesting a low void nucleation tendency. The XRM analysis (Fig. 8(d)) further showed a very low void fraction supporting very sluggish void nucleation (volume fraction of voids as 1.6 %) whereas the 3D reconstructed gauge volume displayed very uniform and finer void

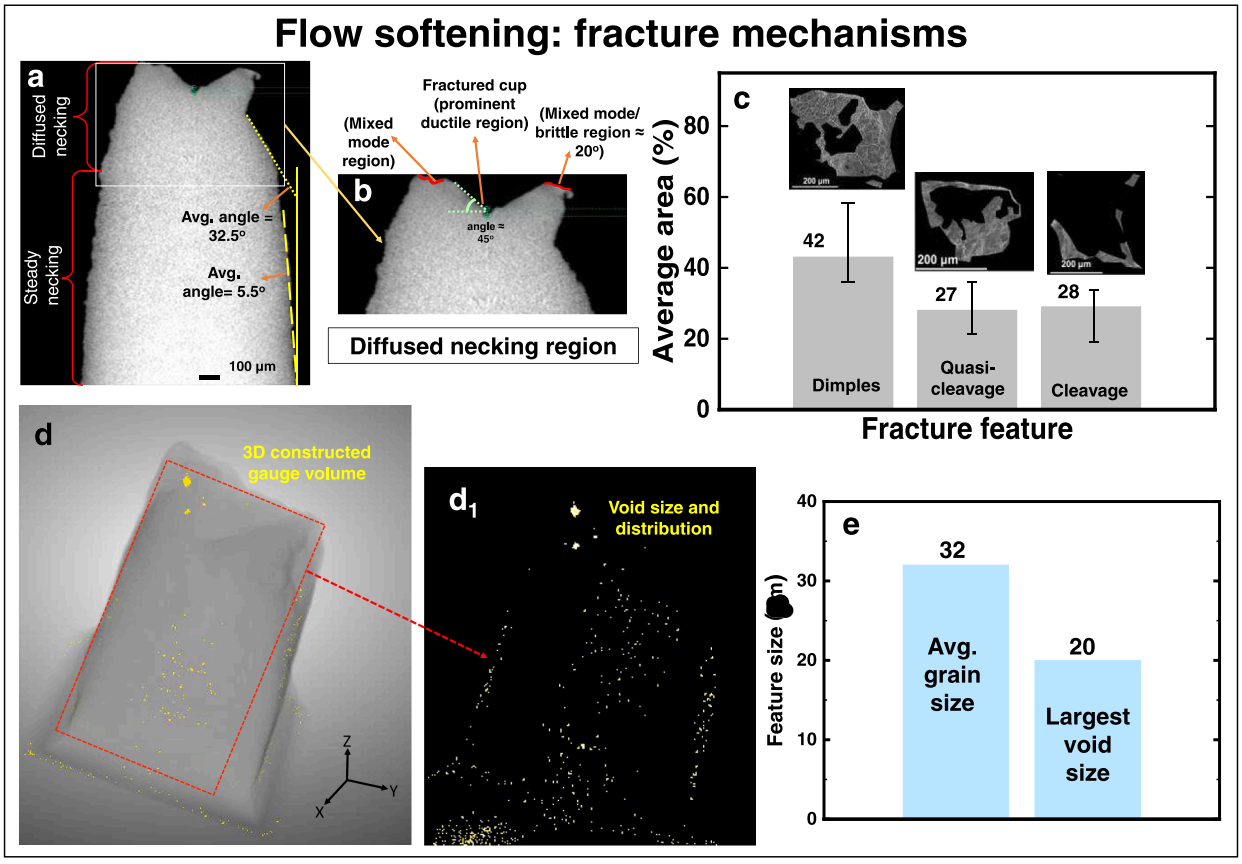

Fig. 8. (a) 2D reconstructed gauge volume of SC Ti-CCA tensile specimen after fracture using X-ray microscopy (XRM) showing diffused necking (b) Cropped section from Fig. 8a showing diffused necking region, (c) Volume fraction analysis of the different fracture modes from the fractographic micrograph, (d, d_1) 3D reconstructed gauge volume of SC Ti-CCA tensile specimen using X-ray microscopy (XRM) showing void size and distribution throughout the gauge region after complete fracture, (e) bar chart showing comparative study of average grain size with maximum void size in the SC Ti-CCA.

size distribution (max size of void = 20 μm, average size of 2 μm) thereby confirming early void growth saturation. Moreover, XRM analysis suggests that the maximum void size formed is smaller than the average grain size (Fig. 8(e)) of the SC Ti-CCA and thus suppresses void growth tendency further as per the ripening theory. Also, the DBs formed during deformation can act as a dislocation obstacle, its propensity to promoting stress triaxiality at DB/matrix interface is low since both DBs and matrix have the same crystal structure. Minor presence of β-Zr (b.c.c.) would also not alter the stress axiality at a greater extent in Ti-CCA due to similar deformation requirements as that of the β-Ti (b.c.c.) matrix. Thus, the formation of equiaxed grains, minor volume fractions of deformation obstacles, and the absence of different crystal structures in the microstructures helped in delaying the plastic instability and thus displayed steady necking assisted flow softening event in the SC Ti-CCA [47,48].

3.5. Excellent specific strength-ductility synergy

Fig. 9(a) reproduces Fig. 1(a_4) i.e., SDI vs. VEC plot [12,14–27] with the addition of Ti-CCA data point. It is important to first note that SC Ti-CCA locates itself at a position better than the targeted region which suggests the design philosophy used is a pathway of future design of Ti-based complex alloys. Moreover, the alloy outperforms all existing Ti-based conventional and complex alloys (Ti > 45 at. %) in SDI values in the as-cast state to date. It is further interesting to note that Ti CCA is found to be way better in SDI values compared to the SDI values of alloys having YS > 1 GPa. This suggests the Ti-CCA has the synergistic presence of high SDI and specific YS without any post-processing treatments, which is an ongoing demand of most of the structural material industries in terms of alloy characteristics. This is also supported by the SDI vs. specific yield strength (Fig. 9(b)) plot made for the same data points as shown in Fig. 9(a). Thus, Ti-CCA overcomes the strength-ductility paradigm in the pre-existing Ti alloys by simultaneous inheritance of significant YS, UTS, and ductility in a much cheaper way compared to high-density and high-cost elements (Hf, Ta, and W) containing lightweight refractory CCAs.

4. Conclusions

The design and successful fabrication of $Ti_{50}Zr_{16}V_{16}Nb_{10}Al_5Mo_3$ (Ti-CCA) led to the following conclusions.

1. β-Ti (b.c.c.) dominated as-cast microstructure of Ti-CCA displayed an equiaxed grain structure with heterogenous grain size distribution with minor presence of β-Zr phase (~3%) which is the result of not only selected alloy chemistry but also of the fabrication route.
2. This work's design of Ti-CAA shows a 35 % tensile ductility when compared to traditional Ti-based alloys or newly designed Ti-CCAs while having not only high ultimate tensile strength but also very high yield strength (YS) thereby overcoming the conventional strength-ductility tradeoff without performing any post-processing of the SC microstructure when compared with conventional Ti-based alloys or recently designed Ti dominating CCAs.
3. This synergistic combination of YS, UTS, and ductility is a result of sustained strain hardening response due to the formation of deformation bands (DBs) and work hardening activity at the DB/matrix interfaces occurring concurrently in heterogenous grained β microstructure whereas steady softening response as a result of delayed void nucleation and its early growth saturation in heterogenous equiaxed grain microstructure.
4. The multi-filtering (merging CCA design, VEC, solubility, and density concepts) alloy design approach used in the current work for the development of Ti-CCA provided a new pathway for realizing next-generation, strong, and ductile CCAs cost-effectively.

CRediT authorship contribution statement

A.R. Balpande: Writing – review & editing, Investigation, Formal analysis, Data curation, Conceptualization. **S. Agrawal:** Writing – review & editing, Investigation, Data curation. **X. Li:** Writing – review & editing, Investigation, Data curation. **S. Suwas:** Writing – review & editing, Investigation, Data curation. **S. Guo:** Writing – review & editing, Investigation, Data curation. **P. Ghosal:** Writing – review & editing, Investigation, Data curation. **S.S. Nene:** Writing – original draft, Supervision, Project administration, Methodology, Funding acquisition, Formal analysis, Data curation, Conceptualization.

Declaration of competing interest

The authors declare that they have no known competing financial interests or personal relationships that could have appeared to influence the work reported in this paper.

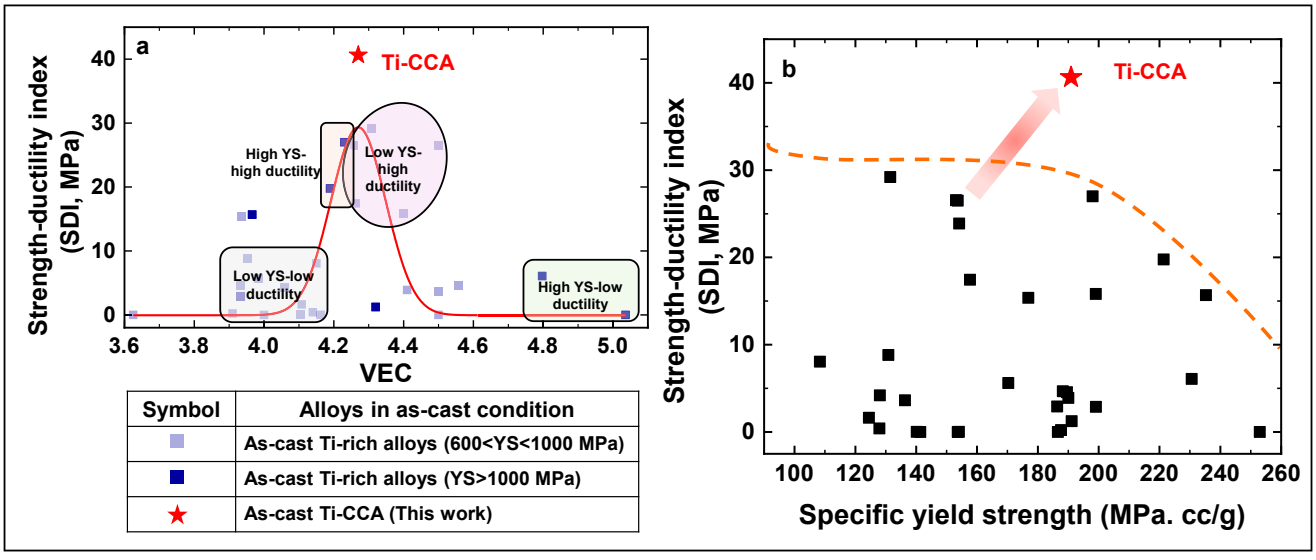

Fig. 9. (a) Strength-ductility index vs VEC, (b) Strength-ductility index vs specific yield strength of the designed alloy in comparison with the pre-existing as-cast Ti-rich alloys [12,14–27].

Data availability

Data will be made available on request.

Acknowledgments

SSN would like to acknowledge the financial support received from the seed grant (I/SEED/JVS/SN/20200077) issued by the Indian Institute of Technology Jodhpur and the start-up grant (S/SERB/SN/20210069) by the Science and Engineering Research Board (SERB), India towards the purchase of a vacuum electric arc melting furnace and the raw material respectively. The authors are very thankful to Prof. R.S Mishra and Dr. Ravi Sankar Haridas from the University of North Texas, USA for performing the X-ray microscopy (XRM) experiments and Mr. Nagarajun Sridhar from Zeiss, India for helping in the analysis of XRM results.

Appendix A. Supplementary data

Supplementary data to this article can be found online at https://doi.org/10.1016/j.matdes.2024.112988.

References

[1] T. Zhang, Z. Huang, T. Yang, H. Kong, J. Luan, A. Wang, D. Wang, W. Kuo, Y. Wang, C.-T. Liu, In situ design of advanced titanium alloy with concentration modulations by additive manufacturing, Science 374 (2021) 478–482.
[2] C.A.F. Salvador, V.C. Opini, M.G. Mello, R. Caram, Effects of double-aging heat-treatments on the microstructure and mechanical behavior of an Nb-modified Ti-5553 alloy, Mater. Sci. Eng. A. 743 (2019) 716–725.
[3] J. Chen, L. Yan, S. Liang, X. Cui, C. Liu, B. Wang, L. Zou, Remarkable improvement of mechanical properties of layered CNTs/Al composites with Cu decorated on CNTs, J. Alloys Compd. 901 (2022) 163404.
[4] H. Ding, X. Cui, Y. Zhang, Z. Wang, N. Gao, T. Zhang, J. Luo, X. Zhai, J. Chen, L. Geng, L. Huang, Int. J. Plast. 171 (2023) 103805.
[5] B. Lin, X. Chen, J. Chen, S. Chen, R. Lu, S. Liang, X. Cui, H. Chi, L. Zou, J. Mater. Res. Technol. 24 (2023) 9928–9938.
[6] H. Huang, Y. Wu, J. He, H. Wang, X. Liu, K. An, W. Wu, Z. Lu, Phase-Transformation Ductilization of Brittle High-Entropy Alloys via Metastability Engineering, Adv. Mater. 29 (30) (2017) 1701678.
[7] O.N. Senkov, D.B. Miracle, K.J. Chaput, Development and exploration of refractory high entropy alloys—A review, J. Mater. Res. 33 (2018) 3092–3128.
[8] C.C. Chung, S.W. Wang, Y.C. Chen, C.P. Ju, J.H.C. Lin, Effect of cold rolling on structure and tensile properties of cast Ti–7.5 Mo alloy, Mater. Sci. Eng. A. 631 (2015) 52–66.
[9] L. Lilensten, J.P. Couzinie, J. Bourgon, L. Perriere, G. Dirras, F. Prima, I. Guillot, Design and tensile properties of a bcc Ti-rich high-entropy alloy with transformation-induced plasticity, Mater. Res. Lett. 5 (2) (2016) 1–7.
[10] Q. Wang, C. Dong, P.K. Liaw, Structural Stabilities of β-Ti Alloys Studied Using a New Mo Equivalent Derived from [β/(α + β)] Phase-Boundary Slopes, Metall. Mater. Trans. A. 46A (2015) 3440.
[11] S. Guo, C. Ng, J. Lu, C.T. Liu, Effect of valence electron concentration on stability of fcc or bcc phase in high entropy alloys, J. Appl. Phys. 109 (2011) 103505.
[12] T. Zhang, J. Zhu, T. Yang, J. Luan, H. Kong, W. Liu, B. Cao, S. Wu, D. Wang, Y. Wang, C.-T. Liu, A new α+ β Ti-alloy with refined microstructures and enhanced mechanical properties in the as-cast state, Scr. Mater. 207 (2022) 114260.
[13] Handbook on, Alloy Phase Diagrams, ASM International, Vol. 3, (1992).
[14] Y. Xu, Z. Liu, X. Zhu, Z. Jiang, H. Chen, N. Wang, Effect of rare earth Ce addition on microstructure and mechanical properties of titanium alloy Ti-6Al-4V, Mater. Lett. 133244 (2023) 330.
[15] D. Li, Y. Dong, Z. Zhang, Q. Zhang, S. Chen, N. Jia, H. Wang, B. Wang, K. Jin, Y. Xue, Y. Dou, X. He, W. Yang, L. Wang, H. Cai, An as-cast Ti-V-Cr-Al light-weight medium entropy alloy with outstanding tensile properties, J. Alloys Compd. 877 (2021) 160199.
[16] N.A. Moshokoa, M.L. Raganya, R. Machaka, M.E. Makhatha, B.A. Obadele, The effect of molybdenum content on the microstructural evolution and tensile properties of as-cast Ti-Mo alloys, Mater. Today Commun. 27 (2021) 102347.
[17] S.H. Hong, Y.J. Hwang, S.W. Park, C.H. Park, J.T. Yeom, J.M. Park, K.B. Kim, Low-cost beta titanium cast alloys with good tensile properties developed with addition of commercial material, J. Alloys Compd. 793 (2019) 271–276.
[18] Y.C. Liao, T.H. Li, P.H. Tsai, J.S.C. Jang, K.C. Hsieh, C.Y. Chen, J.C. Huang, H. J. Wu, Y.C. Lo, C.W. Huang, I.Y. Tsao, Intermetallics 117 (2020) 106673.
[19] C.D. Yang, S.P. Wang, J.J. Shi, C.H. Wang, Z.M. Ren, G.H. Cao, Microstructures and mechanical properties of as-cast titanium–zirconium–molybdenum ternary alloys, Mat. Wiss. u. Werkstofftech. 49 (2018) 30–38.
[20] C. Xia, X. Zhang, S. Liu, B. Chen, C. Tan, X. Zhang, M. Ma, R. Liu, Thermo-mechanical processing, microstructure and mechanical properties of TiZrB alloy, Mater. Sci. Eng. A. 712 (2018) 350–357.
[21] Y. Yu, Y.H. Cai, X.H. Chen, T. Wang, Y.D. Wu, J.J. Si, X.D. Hui, A high strength and elastic carbon containing near-α Ti alloy prepared by hot isostatic pressing process, Mater. Sci. Eng. A. 651 (2016) 961–967.
[22] K. Li, X. Liu, Y. Liu, X. Wu, W. Zhang, J. Yang, W. Li, S. Zhou, Strengthening layer with nano-twins in titanium alloy induced by laser surface re-melting: Mechanism of high strength and ductility, Mater. Charact. 196 (2023) 112632.
[23] K.M. Li, Y.J. Liu, X.C. Liu, X. Wu, S.F. Zhou, L.C. Zhang, W. Li, W.C. Zhang, Simultaneous strength-ductility enhancement in as-cast Ti6Al4V alloy by trace Ce, Mater. Des. 215 (2022) 110491.
[24] S. Zhou, P. Peng, Y. Xu, X. Zhang, Z. Ma, J. Yang, J. Wang, Investigation on microstructure and mechanical properties of heat-treated Ti-47.5 Al–3Nb-3.5 Cr alloy, Mater. Sci. Eng. A. 832 (2022) 142366.
[25] I.V. Okulov, U. Kuhn, T. Marr, J. Freudenberger, I.V. Soldatov, L. Schultz, C. G. Oertel, W. Skrotzki, J. Eckert, Microstructure and mechanical properties of new composite structured Ti–V–Al–Cu–Ni alloys for spring applications, Mater. Sci. Eng. A. 603 (2014) 76–83.
[26] W. Lai, H. Liu, X. Yu, Y. Yi, W. Li, S. Zhou, S. Cui, X. Wang, A design of TiZr-rich body-centered cubic structured multi-principal element alloys with outstanding tensile strength and ductility, Mater. Sci. Eng. A. 813 (2021) 141135.
[27] S. Zeng, Y. Zhou, H. Li, H. Zhang, H. Zhang, Z. Zhu, Microstructure and mechanical properties of lightweight Ti3Zr1.5NbVAlx (x= 0, 0.25, 0.5 and 0.75) refractory complex concentrated alloys, J. Mater. Sci. Technol. 130 (2022) 64–74.
[28] S. Thapliyal, P. Agrawal, P. Agrawal, S.S. Nene, R.S. Mishra, B.A. McWilliams, K. C. Cho, Segregation engineering of grain boundaries of a metastable Fe-Mn-Co-Cr-Si high entropy alloy with laser-powder bed fusion additive manufacturing, Acta Mater. 219 (2021) 117271.
[29] S. Kou, Welding metallurgy, Second Edition, 2003.
[30] J. Wang, S. Bai, Y. Tang, S. Li, X. Liu, J. Jia, Y. Ye, L. Zhu, Effect of the valence electron concentration on the yield strength of Ti–Zr–Nb–V high-entropy alloys, J. Alloys Compd. 868 (2021) 159190.
[31] S. Gangireddy, B. Gwalani, V. Soni, R. Banerjee, R.S. Mishra, Contrasting mechanical behavior in precipitation hardenable Al_XCoCrFeNi high entropy alloy microstructures: Single phase FCC vs. dual phase FCC-BCC, Mater. Sci. Eng. A. 739 (2019) 158–166.
[32] M. Naeem, H. He, F. Zhang, H. Huang, S. Harjo, T. Kawasaki, B. Wang, S. Lan, Z. Wu, F. Wang, Y. Wu, Z. Lu, Z. Zhang, C.T. Liu, X.L. Wang, Cooperative deformation in high-entropy alloys at ultralow temperatures, Sci. Adv. 6 (4002) (2020) 1–8.
[33] Z. Fu, B.E. MacDonald, Z. Li, Z. Jiang, W. Chen, Y. Zhou, E.J. Lavernia, Engineering heterostructured grains to enhance strength in a single-phase high-entropy alloy with maintained ductility, Mater. Res. Lett. 6 (11) (2018) 634–640.
[34] S. Sheikh, S. Shafeie, Q. Hu, J. Ahlstrom, C. Persson, J. Vesely, J. Zyka, U. Klement, S. Guo, Alloy design for intrinsically ductile refractory high-entropy alloys, J. Appl. Phys. 120 (2016) 164902.
[35] S. Banerjee, P. Mukhopadhyay, Phase Transformations: Examples from Titanium and Zirconium Alloys 12 (2007) 1–813.
[36] A. Mantri, D. Choudhuri, A. Behera, M. Hendrickson, T. Alam, R. Banerjee, Role of isothermal omega phase precipitation on the mechanical behavior of a Ti-Mo-Al-Nb alloy, Mater. Sci. Eng. A. 767 (2019) 138397.
[37] A.C. Lewis, S.M. Qidwai, A.B. Geltmacher, Slip systems and initiation of plasticity in a body-centered-cubic titanium alloy, Metall. Mater. Trans. A. 41A (2010) 2522.
[38] B. Verlinden, J. Driver, I. Samajdar, R.D. Doherty, Thermo-Mechanical Processing of Metallic Materials, Pergamon Materials Series, Oxford.
[39] S.S. Nene, S. Sinha, M. Frank, K. Liu, R.S. Mishra, B.A. McWilliams, K.C. Cho, Unexpected strength–ductility response in an annealed, metastable, high-entropy alloy, Appl. Mater. Today 13 (2018) 198–206.
[40] S.S. Nene, M. Frank, K. Liu, R.S. Mishra, B.A. McWilliams, K.C. Cho, Extremely high strength and work hardening ability in a metastable high entropy alloy, Sci. Rep. 8 (2018) 9920.
[41] E. Welsch, D. Ponge, S.M.H. Haghighat, S. Sandlobes, P. Choi, M. Herbig, S. Zaefferer, D. Raabe, Strain hardening by dynamic slip band refinement in a high-Mn lightweight steel, Acta Mater. 116 (2016) 177–199.
[42] H.S. Arora, A. Ayyagari, J. Saini, K. Selvam, S. Riyadh, M. Pole, H.S. Grewal, S. Mukherjee, High Tensile Ductility and Strength in Dual-phase Bimodal Steel through Stationary Friction Stir Processing, Sci. Rep. 9 (2019) 1972.
[43] H. Ding, X. Cui, Z. Wang, T. Zhao, Y. Wang, Y. Zhang, H. Chen, L. Huang, L. Geng, J. Chen, A new strategy for fabrication of unique heterostructured titanium laminates and visually tracking their synchronous evolution of strain partitions versus microstructure, J. Mater. Sci. Technol. 107 (2022) 70–81.
[44] Z. Wang, X. Cui, L. Chen, Y. Zhang, H. Ding, Y. Zhang, N. Gao, G. Cong, Q. An, S. Wang, J. Chen, L. Geng, L. Huang, Mater. Sci. Eng. A. 891 (2024) 145926.
[45] S. Sinha, S.S. Nene, M. Frank, K. Liu, R.A. Lebensohn, R.S. Mishra, Deformation mechanisms and ductile fracture characteristics of a friction stir processed transformative high entropy alloy, Acta Mater. 184 (2020) 164–178.
[46] ASM Handbook on, Failure Analysis and Prevention 11 (2002).
[47] H.G.F. Wilsdorf, Void initiation, growth and coalescence in ductile fracture of metals, J. Electron. Mater. 4 (5) (1975) 792–809.
[48] D. Lassance, F. Scheyvaerts, T. Pardoen, Growth and coalescence of penny-shaped voids in metallic alloys, Eng. Fract. Mech. 73 (2006) 1009–1034.